# An XRD/XRF instrument for the microanalysis of rocks and minerals

S Cornaby[1], A Reyes-Mena[1], H K Pew[1], P W Moody[1], T Hughes[2], A Stradling[2], D C Turner[1] and L V Knight[2]

[1] MOXTEK, Inc., 452 West 1260 North, Orem, UT 84057, USA
[2] Department of Physics and Astronomy, Brigham Young University, Provo, UT 84602, USA

E-mail: areyes@moxtek.com and larry_knight@byu.edu

**Abstract**
A breadboard setup constructed at MOXTEK, Inc., is capable of capturing both x-ray diffraction (XRD) and x-ray fluorescence (XRF) information simultaneously using a charge-coupled device (CCD) as the x-ray detector. This preliminary setup will lead to a prototype simultaneous XRD/XRF instrument. NASA is funding the instrument's construction because of its capabilities and small size; it could be used for future Mars missions for analysis of rocks. The instrument uses a CCD to capture both the energy and the spatial information of an incoming x-ray. This is possible because each pixel acts as a spatially addressable energy-dispersive detector. A powdered sample of material is placed in front of the CCD, which in turn is bombarded by a collimated x-ray beam. The instrument's critical features—namely the x-ray source, collimation optics and x-ray transparent windows—allow for the first time, to the best of our knowledge, mounting the sample outside the CCD camera. In this paper the instrument's design parameters as well as the properties of both a front-side-illuminated (FSI) CCD and back-side-illuminated (BSI) CCD as x-ray detectors are investigated.
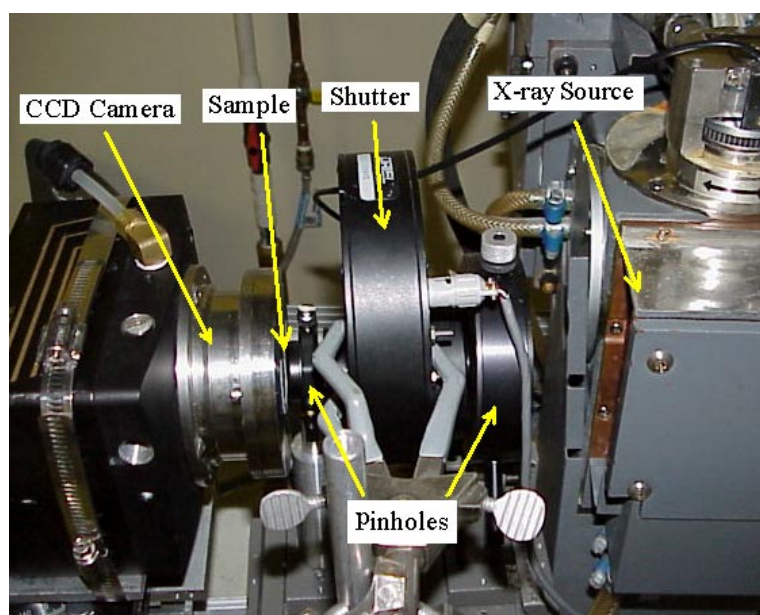
**Keywords:** x-ray diffraction (XRD), x-ray fluorescence (XRF), charged-coupled device (CCD), compact instrument, powdered diffraction, Mars, back-side illuminated CCD, front-side illuminated CCD, energy-dispersive detector

## 1. Introduction

A first prototype x-ray diffraction (XRD)/x-ray fluorescent (XRF) instrument was developed at Ames National Laboratory and is currently in use at Los Alamos National Laboratory [1, 2]. The intended applications for this instrument are for planetary exploration and as a portable instrument for terrestrial use. NASA funding for the instrument's construction is based on its possible use in future Mars missions. These missions have previously only used methods that give elemental composition, which are subject to sizable uncertainties for mineral identification. XRF gives the elemental composition and suggests certain minerals, but the traditional well tested method of definitive mineral identification is by XRD [3]. With a small, portable XRD/XRF instrument, both the diffraction and the fluorescence information can be feasibly gathered on Mars as well as on Earth.

The purpose of the breadboard setup constructed at MOXTEK is to incorporate and test some of the various key components involved in an XRD/XRF instrument design. This has allowed samples to be placed on the outside of the camera so that they can be easily retrieved and exchanged. The information gained from this breadboard will lead to a prototype instrument, which will be small and portable when a final design is completed. In this paper all the components and their functions will be described, and the advantages and limitations will be discussed.

The key component of the instrument is the CCD detector. It can use each pixel as an addressable individual energy-dispersive detector, so the spatial position and the energy of an x-ray event can be simultaneously recorded. Once all the events are recorded, the diffraction information and the fluorescent information can be extracted with the use of sorting algorithms [4]. We have investigated some of the properties of both a front-side-illuminated (FSI) CCD and a

**Figure 1.** Picture of the breadboard instrument.

back-side-illuminated (BSI) CCD, such as energy resolution and detection limits. In particular, one key feature investigated was the rate at which the CCD camera records single x-ray events. It is critical that the camera be able to capture events into single pixels effectively enough to be used as an energy-dispersive detector and, thereby, be useful for the XRD/XRF instrument.

## 2. Experimental setup

The breadboard setup for simultaneously capturing both XRF and XRD consists of a commercial CCD camera, an x-ray tube, a beam collimating system made up of pinholes, a shutter, and a sample support. Figure 1 shows the breadboard instrument, where the major components can be seen. The x-rays are collimated, and then irradiate the sample mounted outside the CCD camera. The CCD camera is used to collect the scattered x-rays. The placement of the sample in relation to the CCD is critical in order for a diffraction pattern to be captured. All of the components are kept as close together as possible to achieve a high x-ray flux. A vacuum environment is maintained inside the camera with the use of x-ray transparent MOXTEK DuraBeryllium™ and UltraThin™ polymer AP1.3 windows [5] mounted on the camera flange. The next eight sections explain all the components, except for the CCDs, of the breadboard instrument in detail.

### 2.1. The x-ray source

The breadboard x-ray source consists of a high brilliance 'Rotaflex' Rigaku rotating copper anode x-ray tube (model RU-200) capable of generating a fairly well collimated 1 mm by 0.1 mm x-ray beam. The tube was operated at 30 kV and 30 mA for most of the XRF and XRD data collected. The tube is housed in a radiation shield and is immovable with reference to the table on which it resides. This tube was used because

of its availability to us. The final instrument will need a much smaller, low powered x-ray tube.
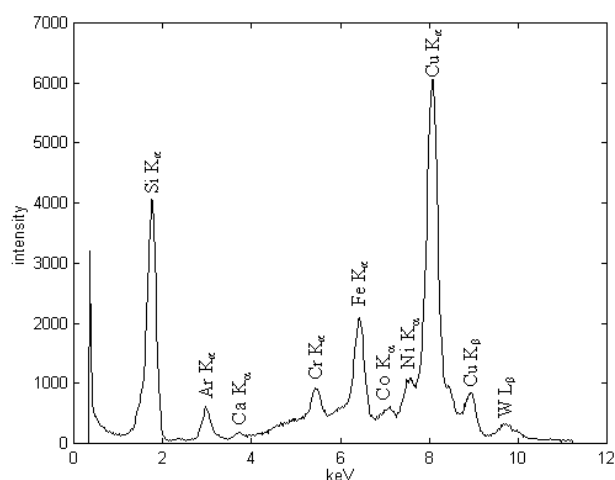
The x-ray source that will be employed in future versions of the instrument will be a field-emitter x-ray tube, which is being built at MOXTEK [6]. This tube will have a highly focused and intense x-ray spot. The tube will be powered by 3 W or less and be 4 cm long, weighing 50 grams. It will generate a comparable intensity of x-rays, allowing the instrument to be small and portable.

### 2.2. Collimation optics

The x-rays are collimated with a 100 $\mu$m tungsten pinhole and a 300 $\mu$m lead pinhole. Lead and tungsten are the materials used for the two collimating pinholes because of their x-ray blocking characteristics in the CCD detection range of 1 to 10 keV (section 3.2) and they are readily available. A beam spot with a diameter of 150 $\mu$m or less is preferred to obtain recognizable diffraction patterns. The pinholes are aligned by means of a laser beam and $XZ$ stages. In the present geometry the pinholes are spaced 9.5 cm apart. The full angular spread of the collimated beam has been measured to be less than $0.3°$. The CCD camera flange is placed in contact with the 100 $\mu$m tungsten pinhole mount in order to capture more counts per exposure to the CCD.

This pinhole plays a factor in the fluorescent noise in the energy spectrum and may cause noise in the diffraction patterns. Fluorescent noise is caused by a fluorescent x-ray that is excited by the source but is not fluoresced off the sample. The Cu $K_\alpha$ (8.012 keV) line used to capture the diffraction lies within the same region as the W $L_\alpha$ (8.396 keV) line. A small W $L_\beta$ (9.670 keV) line can be seen in most of the samples that have been studied (figure 2)[3]. The W $L_\alpha$ line is difficult to

---

[3] Figure 2 also shows other fluorescent noise from various components in the instrument. The Fe, Co, Ni and Cr $K_\alpha$ lines come from the metals in the flange and shutter, the Cu $K_\alpha$ and $K_\beta$ lines come from the x-ray source, the Ar $K_\alpha$ line is from the air, and both the Si $K_\alpha$ line and the small Ca line $K_\alpha$ are from the sample.

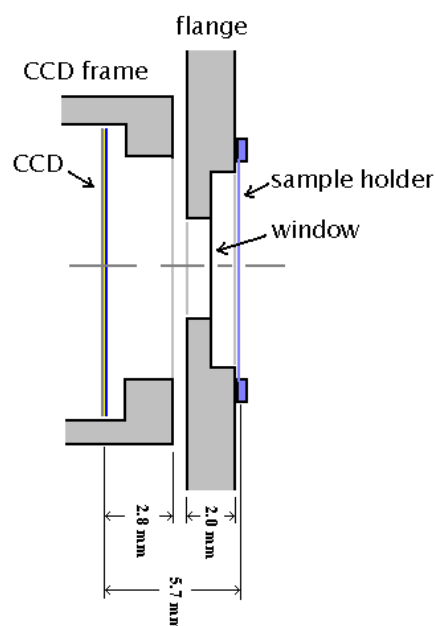**Figure 2.** XRF spectra with tungsten L$_\beta$ peak (collected from a quartz sample).

observe because of its relatively low counts compared to those of the Cu K$_\alpha$ line. Also, the energy resolution of the CCD in this region is about 0.32 keV (section 3.1), making it difficult to resolve the peaks. Pinholes of other materials may decrease the noise in the XRD information by fluorescing at an energy far removed from the energies fluoresced from the source. For example, pinholes constructed from a platinum–iridium alloy would eliminate fluorescent noise from the pinholes in the diffraction patterns because none of the characteristic energies from these elements are near to the Cu K$_\alpha$ line.

### 2.3. The shutter

The shutter's function is to stop the x-ray flux during the readout cycle of the CCD, and it can be placed anywhere between the camera and the source. The shutter is lined with lead to make it effective in blocking x-rays. Without the shutter, the CCD is exposed during readout; this causes the image to smear in the direction of the readout. This smearing has mostly been corrected with the shutter; but a small amount still occurs because our camera-control box shutter timing is nonadjustable. However, this small amount of smearing has not seemed to affect the quality of the data captured at the present data collection rate. The exposure time of the CCD to x-rays is about five seconds while there is only an estimated tenth of a second exposure time during readout out of the total readout time of two and a half seconds. This does not allow enough exposure time during readout to see smearing effects in the diffraction images.

### 2.4. The geometry of the CCD flange

The present geometry of the camera flange is based on getting the sample as close to the CCD as possible, which allows more of the diffraction pattern to be captured (section 3.4). The total distance between the sample and the CCD is 5.7 mm. The instrument was also designed to keep the sample on the outside of the camera. This design allows us to easily retrieve and exchange samples. To keep the CCD vacuum integrity a window is placed between the sample and the CCD. Figure 3 shows a diagram of the various component placements. The
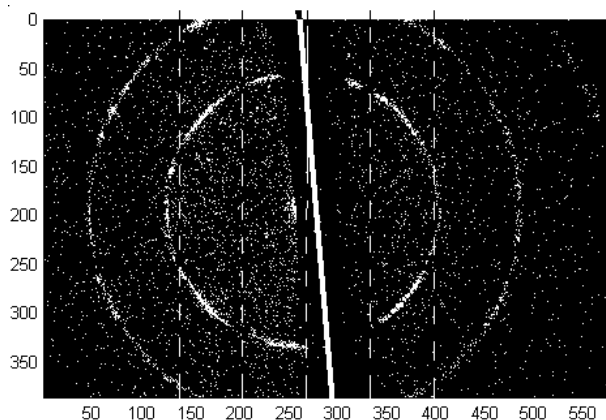


**Figure 3.** Diagram of the CCD and CCD flange.

CCD itself is housed in a frame that contains the electrical contacts with their radiation shielding. A stainless steel flange holds the window and supports the sample holder. The distance between the flange and the framework of the CCD is 0.5 mm. This space is needed because the CCD is cooled and cannot be in contact with the flange. There also must be a sufficient room for a beam-stop (next section) to be placed behind the window on the flange. The sample holder itself causes the sample to be spaced 0.4 mm in front of the flange. The design of the flange and the camera allow the diffraction information to be captured with the sample being outside the camera.
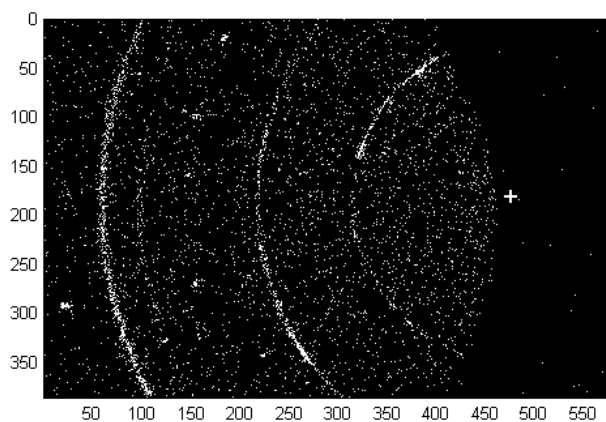
### 2.5. Beam-stops

To prevent damaging the CCD, non-scattered x-rays need to be blocked with a 'beam-stop'. A beam-stop blocks the direct beam but does not block the diffracted and fluorescent radiation. The beam-stops we presently use are the 1 mm thick stainless steel edge of the camera flange and an approximately 0.3 mm thick, 0.5 mm wide lead wire. The lead beam-stop can be seen in figure 4 as a vertical line where no x-ray events occur in the diffraction pattern. This beam-stop is placed vertically inside the camera and is mounted on the flange directly behind the window. A translation stage moves the camera, allowing the beam-stop to be precisely positioned in the beam line. The advantage of using a beam-stop to block the central spot of the CCD is that full diffraction rings characteristic of powdered samples can be captured.

A diffraction pattern using the camera flange as a beam-stop can be seen in figure 5. This is done by positioning the sample and the incident beam outside the field of view of the CCD. Using the edge of the flange has the advantage of allowing larger 2$\theta$ angles to be captured but it complicates the determination of the relative diffraction peak intensities. The relative intensities of the diffraction peaks are particularly useful for mineral identification.

**Figure 4.** X-ray diffraction pattern using an AP1 window and the lead wire beam-stop (collected from a NaCl sample). The window silicon ribs are located on the dotted lines and the beam-stop is located on the solid line.
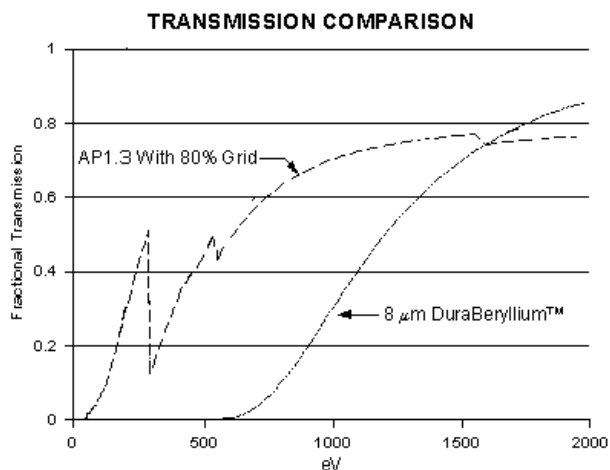


**Figure 5.** X-ray diffraction pattern using a beryllium window and the camera flange as the beam-stop (collected from a NaCl sample). The edge of the window can be seen in the x-ray shadow. The cross gives the location of the beam spot.

### 2.6. CCD camera windows and the sample holder

In previous prototype XRD/XRF instruments the CCD camera houses not only the CCD detector, but also the sample to be analysed. Consequently, the process of retrieving and changing samples becomes a cumbersome and time-consuming operation. Having the sample on the outside of the camera greatly simplifies sample handling. In order to achieve this, an x-ray window has to be placed between the CCD and the sample. The window and the sample holder need to be transparent over the full range of sensitivity of the CCD. The two types of window that we have tested are beryllium foils and MOXTEK AP1 windows. The windows' range of transparency in the soft x-ray region is given in figure 6 [5]. The windows used have an effective area of 18 mm$^2$.

#### 2.6.1. Beryllium windows and beryllium diffraction.
DuraBeryllium$^{TM}$ foil windows were first used as windows on the CCD flange. The windows consist of an 8 $\mu$m thick beryllium foil with a 1 $\mu$m refractory low-$Z$ coating which makes the window leak tight and resilient. These windows have shown adequate transparency for the detection range



**Figure 6.** The transmission efficiency of the x-ray windows.

of the FSI CCD presently being used. Nevertheless, there are a few problems that have been found with the beryllium windows. One is that fluorescent x-rays from light elements ($Z < 12$) are absorbed in the beryllium window. Another is that the beryllium window itself causes a diffraction pattern. We discovered the beryllium diffraction pattern while trying to identify an unknown sample. There was an obvious discrepancy in comparing the diffraction patterns obtained using a commercial diffractometer and our CCD instrument. The diffraction pattern is present because the beryllium foil is very thick compared to the x-ray wavelength of 1.54 Å. The foil is made up of many randomly oriented crystals, just like the samples, so a ring pattern is observed. The diffraction pattern would not be present if the collimated beam were blocked before it reached the beryllium window. Using the flange edge as the beam-stop eliminates this diffraction pattern. Another solution to this problem is to have the lead beam-stop in front of the beryllium window. This will stop the x-ray beam before the beryllium foil can diffract it.

#### 2.6.2. AP1 windows.
The AP1 window transmits x-rays at lower energies and therefore has a wider transmission range. These windows are constructed of a thin polymer material supported by a silicon-rib structure to reinforce it against pressure gradients. The AP1 film consists of alternating layers of the AP1 polymer and aluminium with a total thickness of 0.30 $\mu$m polymer and 0.040 $\mu$m of aluminium. With these windows we verified that the FSI CCD is not sensitive to softer x-rays (section 3.1).

There are some problems caused by the silicon-rib structure that supports the AP1 window. The diffracted events at 8.01 keV are partially blocked by the rib structure causing vertical lines of weak intensities. This causes the spotty look of the rings in figure 4. Fluorescent x-rays at lower energies are entirely blocked by the rib structure.

#### 2.6.3. AP1 sample holders.
The sample holders being used are AP1 films without any rib structure. The films are excellent supports for the sample because of their x-ray transparent qualities. A powdered sample is fixed to the support by a small amount of vacuum grease (silicon or graphite). The

sample is then placed in front of the camera so that the x-rays will irradiate the sample.

## 3. CCD capabilities and results

Two Princeton Instruments CCD cameras were used in order to compare the fluorescent information collected. One camera has an FSI CCD (consisting of an EEV CCD02 576 × 384 CCD with 22 $\mu$m × 22 $\mu$m pixels and an active area of 8.4 mm × 12.7 mm) and the other has a BSI CCD (consisting of an EEV 512 × 512 CCD with 25 $\mu$m × 25 $\mu$m pixels and an active area of 12.7 mm × 12.7 mm).
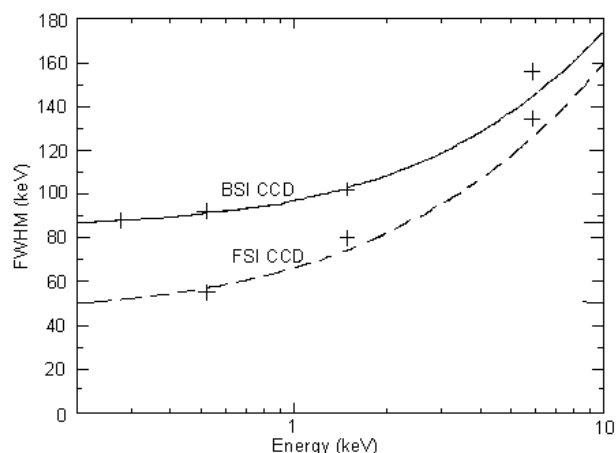
Along with others [7–9] we have investigated the basic characteristics of both FSI and BSI CCDs in the x-ray region. Within the CCD industry there is an ever-growing effort to optimize the sensitivity, resolution, timing and readout speed of a CCD. Finding the right CCD for the XRD/XRF instrument is the key to making a useful and fast instrument. The construction of FSI CCD is such that radiation must pass through the gate structure in order to enter the depletion region where the radiation is detected. The gate structures are in front of the depletion region because of the fabrication process, and for customary regions of detection the gate structures are largely transparent [10]. The BSI CCD was developed in an effort to increase the range and sensitivity of CCDs. This device has the supporting silicon wafer etched away until the depletion region is reached. The radiation is exposed to the backside where there is no interference from the gate structure. This increases the sensitivity and range of the CCD because the radiation does not have to pass through any other structures [10]. The next four sections give the properties of the two types of CCDs. In comparing the properties of the two types of CCDs, we have found that the FSI CCD is best suited for use in a simultaneous XRD/XRF instrument.

### 3.1. Energy resolution

The energy resolution of different types of CCDs has been explored experimentally and researched in the literature [7, 8]. The major factors that control the resolution of both of the CCDs are temperature and exposure time. The Fano factor limits the energy resolution displayed in figure 7, but in order to reach this limit the dark current noise must be substantially decreased by operating the CCD at lower temperatures. Decreasing the temperature improves the energy resolution to the Fano factor limitation. Decreasing the exposure time also increases the energy resolution, but at lower temperatures the exposure time becomes a less significant effect on the resolution of the CCD.

The FSI CCD is cooled with a thermoelectric cooler aided by water cooling. Table 1 contains the energy resolution for the FSI device at various energies at a temperature of −50 °C for a 5 to 8 second exposure time. At this temperature, the energy resolution is adequate to discriminate between the $K_\alpha$ and $K_\beta$ peaks above 3.6 keV (calcium) in the energy spectra.

Energy resolution degrades at higher temperatures in the CCD due to thermal noise. This noise is measured as the number of electron–hole pairs created per second or counts per second (cps). For each decrease of 6 to 7 °C in the temperature of the CCD, the thermal noise is halved [10]. Table 2 gives



**Figure 7.** The FWHM energy resolution of FSI CCDs and BSI CCDs. The lines give a model of the CCDs and the points give measured values from the CCDs.

**Table 1.** The energy resolution of the FSI CCD.

| Energy (keV) | Resolution (FWHM) at −50 °C (eV) |
|---|---|
| 1.74 (Si K alpha) | 200–220 |
| 2.62 (Cl K alpha) | 220–240 |
| 3.69 (Ca K alpha) | 220–240 |
| 6.40 (Fe K alpha) | 280–300 |
| 8.01 (Cu K alpha) | 300–320 |

**Table 2.** The cps of the FSI CCD at different temperatures.

| Temperature of CCD (°C) | Counts per second on a pixel |
|---|---|
| 25 (room temperature) | 1500–15 000 |
| −30 | 90–100 |
| −40 | 35–40 |
| −50 | 4–8 |
| −100 | 0.0003 |

the cps for different temperatures of the FSI CCD. The limit of cooling that we can now achieve with the FSI CCD camera is −50 °C.

Within the present limits of the breadboard instrument, a longer exposure time will increase the dark current noise on the CCD and cause a decrease in energy resolution. In order to collect the data we need to make 300 to 500 exposures at about 5 to 8 seconds per exposure [4]. Also, it takes 2 to 3 seconds to read out the CCD between exposures. If we were to shorten the exposure time and increase the number of exposures, we would increase the total data-capturing time due to the readout delays. The exposure time needs to be set to optimize the data collection rate [4]. Therefore, the best way to increase the energy resolution is to cool down the CCD to a lower temperature.

We have compared the resolution of the FSI and the BSI CCDs at −30 °C. An Fe[55] source was used and the energy resolution of both CCDs is roughly equal to 330 eV FWHM at 5.9 keV. This was the limit of cooling achievable for the BSI CCD camera so no comparisons were made for lower temperatures. It has been published that the limit of the energy resolution of the FSI CCDs is somewhat better than that of the

BSI CCDs when operated at lower temperatures [7] (figure 7). This information was modelled for the ACIS CCDs in the Chandra X-Ray Observatory.
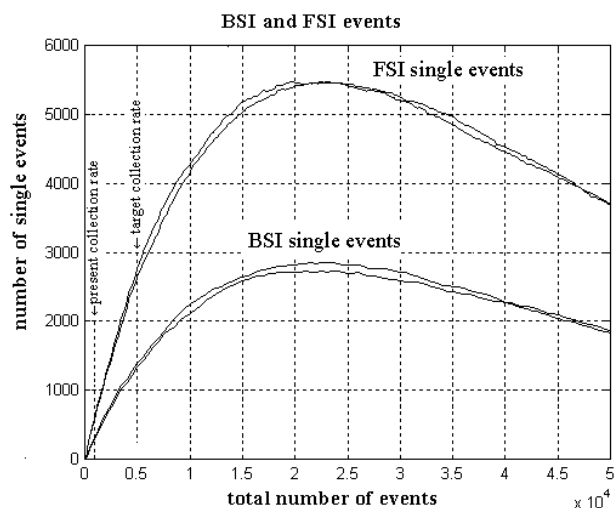
### 3.2. X-ray detection range

The FSI CCD has an x-ray energy detection range from 1.7 keV to 12 keV. A Si $K_\alpha$ peak at 1.7 keV has been seen with the FSI CCD. The FSI CCD has a dead layer, consisting of the gate structure, on the surface that renders poor quantum efficiency at lower energies. At the high end we have detected the Pb $L_\alpha$ line at 10.55 keV. In general CCDs are not able to detect energies far above 11 keV because the active volume of the CCD is not thick enough to absorb all of the harder x-rays' energy. Most of the samples taken are excited by 8.01 keV (Cu $K_\alpha$) x-rays and, consequently, the fluorescent x-rays are below these energies and within the sensitive region of the CCD. BSI CCDs are typically able to detect softer x-rays and therefore are able to detect x-ray energies down to a few hundred eV. The increased sensitivity for soft x-rays is the main advantage that BSI CCDs have over FSI CCDs.

### 3.3. Event types

The major point of comparing FSI and BSI CCDs for applications to a simultaneous XRD/XRF instrument was to find the frequency of single events [4, 11]. As stated earlier, for the instrument to capture useful XRF and XRD information, the energy from one x-ray needs to be captured into one pixel. This type of event is the so-called 'single event'. When one x-ray event is captured in one pixel, then the CCD can be used as an energy-dispersive detector. For the CCD to be used in the single-count mode each of its pixels needs to capture either one event or no events per exposure. If the energy from a single photon is divided into two or more pixels we get a so-called 'split event'. These events are not used; they are discarded from the data set with the use of an algorithm [4].

When comparisons were made, a rhodium x-ray tube was used as the x-ray excitation source. A sample of metal or rock was placed in front of the source and the camera was set up to collect the fluorescent x-rays. We took equal exposure times with each camera. When the images were viewed it was clear that the BSI CCD had far more split events than the FSI CCD. The FSI was able to capture two-thirds of the total events into single pixels, while the BSI CCD was able to only capture one-third of the total events into single pixels. This allowed the FSI CCD to collect more events per exposure then the BSI CCD. At our present collection rate we would need to take 300 to 400 more exposures with the BSI CCD in order to get the same number of counts with the FSI CCD. This would almost double the time required to collect data from a sample.

Figure 8 shows simulations of the FSI and BSI CCDs that give the single-event collection rate per total events collected. As the CCD is exposed to more x-rays the number of single events will eventually decrease. This is because one filled and eight empty pixels are needed in order to have an identifiable single event in our sorting algorithms [4]. At higher count rates there are fewer empty adjacent pixels. Also, in the figure both the present and the target event collection rate are given for a single exposure. There are two main reasons for the location of the target collection rate not being at the maximum of the



**Figure 8.** Modelled single-event collection rate for the FSI and the BSI CCD used in the breadboard.

curve. This represents random x-ray events from fluorescence. The diffraction patterns are not random, therefore they are not represented on the graph. We also want to get a sizeable number of counts at a high collection rate, i.e., we want to collect where the slope is steep [4]. Figure 8 confirms that the FSI CCD is able to gather approximately twice as many single events per exposure than the BSI CCD, when the CCDs are used in single-event count mode.
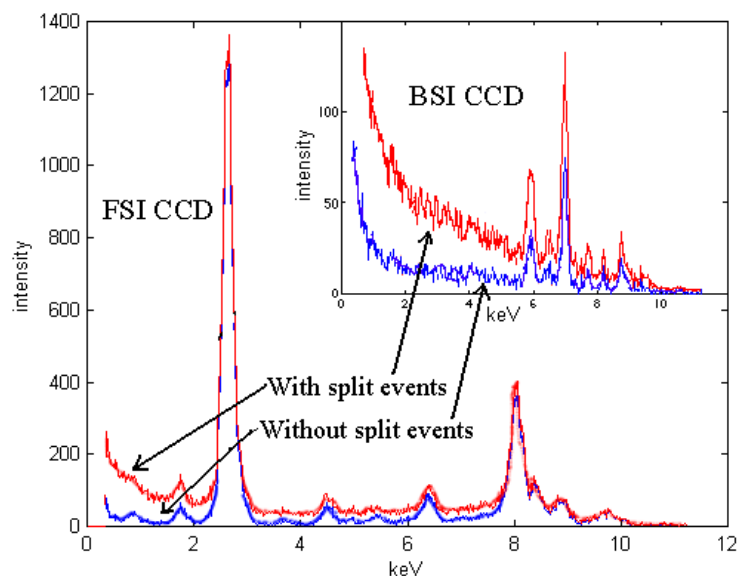
The reason the BSI CCD has a higher rate of split events than the FSI CCD is based on their contrasting structures. The radiation on the FSI CCD is deposited on the same side of the depletion region as the gate structures are located. This causes the pixel boundaries to be well defined because the creation of electron–hole pairs occurs close to the surface of the depletion region. For the BSI CCD the radiation is deposited on the other side of the depletion region where the pixel boundaries are not as well defined since the gate structure is on the other side of this region [7]. It is this structural difference that causes the BSI CCD to have a higher probability for split events.

The higher frequency of split events in the BSI CCD can also be seen by comparing plots in figure 9. These plots show an energy histogram of fluorescent x-ray events collected by the BSI and FSI CCDs. Both graphs show the energy histogram with and without the split events removed. By comparing the plots it can be seen that the BSI CCD has more split events than the FSI CCD. A larger percentage of events needs to be discarded from the BSI spectrum in order to remove the noise caused by split events. This means the BSI has a higher frequency of split events.
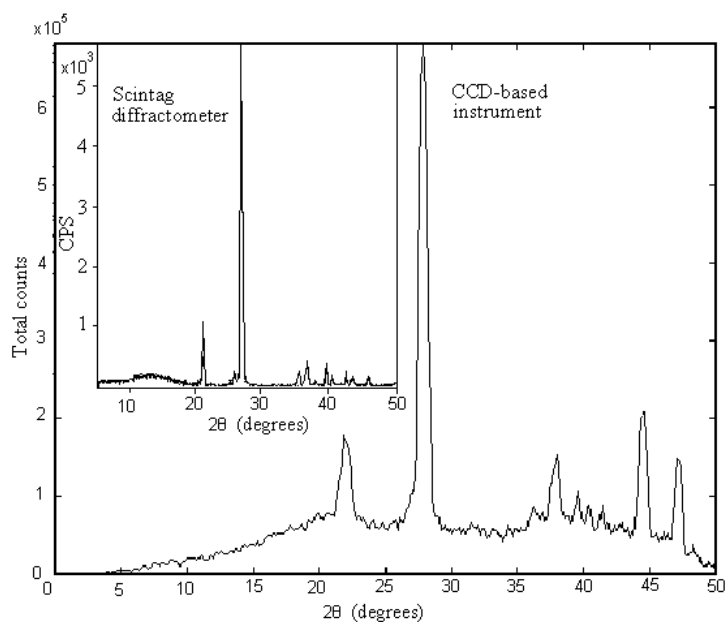
The team that worked on the Chandra X-Ray Telescope has done extensive research on pixel splitting in FSI and BSI CCDs with the same results [7]. They modelled the interaction of x-rays with an FSI CCD, a BSI CCD and an epitaxial FSI CCD using Monte Carlo simulations. Both experiments and models concluded that a FSI CCD has fewer split events than a BSI CCD.

### 3.4. Diffraction range and resolution

The detection range of diffraction of the instrument is based primarily on the distance the sample is from the CCD and

**Figure 9.** X-ray spectrum collected from the FSI CCD (calcite sample) and a BSI CCD (steel sample) with and without split events removed.



**Figure 10.** $2\theta$ diffraction plots captured from a quartz sample with the CCD-based instrument and with a commercial Scintag diffractometer.

the size of the CCD. The range of detection is based on the geometry of the flange on the CCD camera and the size of the FSI CCD. The range of diffraction is measured in $2\theta$, the angle of scattering between the incident beam and the diffracted x-rays. The range of the diffraction peaks captured is 48° $2\theta$ if the beam spot is in the middle of the FSI CCD, however full diffraction rings are not captured out to this angle. Full diffraction rings can be captured out to 37° $2\theta$ based on the width of the CCD. The strongest diffraction peaks of most materials will be seen within 48°. The range of diffraction peaks can be increased to about 65° $2\theta$ if the beam spot is at the edge of the FSI CCD, but full rings will not be captured.

The diffraction resolution in the breadboard instrument is currently limited by the spot size of the incident beam. Our spot size when viewed on the CCD is five pixels across, or about

100 to 120 $\mu$m in size. The beam-spot size is the limiting factor in our angular resolution. The angular resolution FWHM for the breadboard XRD/XRF instrument is approximately 0.4° to 0.7° in a $2\theta$ diffraction plot. This resolution will be able to give the crystal $d$-spacing within ±0.05 Å. The resolution of the diffraction patterns may be slightly improved by using smaller pinholes, but smaller pinholes will reduce the flux of x-rays impinging upon the sample.

Smaller pinholes can, at the most, increase the resolution by a factor of two or three because the limit of resolution is based on the pixel size of the CCD. The limit of angular resolution FWHM for the CCD-based instrument is >0.3° at 0° $2\theta$ and >0.15° at 50° $2\theta$. The resolution is based on the size of the pixels and the present distance of the sample from the CCD. This resolution has not yet been achieved.

## 3.5. XRD/XRF instrument/other methods comparison

A comparison between our CCD-based instrument and a commercially available diffractometer has proven useful to verify our data. Figure 10 contains plots of a diffraction pattern from quartz captured with our instrument and with an XDS-2000 Scintag diffractometer. By comparing these plots, we can see that the major peaks are at the same angle. The two largest peaks have the same relative intensities. The smaller peaks in our instrument are the diffraction from the beryllium window mixed with the quartz diffraction peaks. Either instrument can be used as a mineral identification tool. The CCD-based instrument has the disadvantage of less resolution in the diffraction peaks, but has the advantage of gathering XRF information at the same time, and being much smaller.

## 4. Conclusions

The breadboard XRD/XRF instrument has been successful. XRD and XRF data have been simultaneously gathered from the instrument. We have been able to investigate the various types of event that may occur on both FSI and BSI CCDs. On one hand, it was found that the FSI CCD is more efficient in capturing single events, and is consequently more suitable for an XRD/XRF instrument. On the other hand, the BSI CCD has a larger energy detection range, particularly in the low-energy region. The breadboard's geometrical layout renders a practical device and makes in-air sample analysis possible. The testing setup has been successful in proving the feasibility of a compact XRD/XRF instrument that has the potential to be used in future planetary applications and in terrestrial applications.

## Acknowledgments

## References

[1] Blake D F *et al* 1992 Design of an x-ray diffraction/x-ray fluorescence instrument for planetary applications *Proc. Lunar and Planetary Science Conf. XXIII* pp 117–18
[2] Blake D F *et al* 1993 X-ray diffraction apparatus *US Patent* 5 491 738
[3] Vaniman D, Bish D, Blake D F, Elliott S T, Sarrazin P, Collins S A and Chipera S 1998 Landed XRD/XRF analysis of prime targets in the search for past and present Martian life *J. Geophys. Res.* **103** 31 477–89
[4] Cornaby S, Reyes-Mena A, Pew H K, Moody P W, Hughes T, Stradling A and Knight L V 2000 Using a charged-coupled device (CCD) as an x-ray single photon energy-dispersive detector *J. X-Ray Technol.* at press
[5] MOXTEK 1995 *UltraThin Soft X-Ray Window Data Sheet*
[6] Weal Karian, Knight L V, Allred D and Reyes-Mena A 1993 The use of sharp silicon tips as photocathodes and electron sources for x-ray generation *Nanostruct. Mater.* **3** 419
[7] Nousek J A 1997 *Science Instrument (SI) Operations Handbook for the AXAF CCD Imaging Spectrometer (ACIS)* ACIS-PSU-SOP-01 ver. 2.65, Penn State University, www.astro.psu.edu/xray/docs/sop/sop.html, pp 4.5.1–4.5.3
[8] Prigozhin A, Bautz M, Gendreau K and Ricker G 1996 Calibration of x-ray CCDs with an erect-field grating spectrometer in the 0.2–1.5 keV band *SPIE* **2808** 260–70
[9] Holland A D, Turner M, Abbey A and Pool P 1996 The MOS CCDs for the EPIC on XMM *SPIE* **2808** 414–20
[10] Sweedler J V, Ratzlaff K L and Denton M B (eds) 1994 *Charge-Transfer Devices in Spectroscopy* (New York: VCH) pp 12, 28–9
[11] Lumb D H and Nousek J A 1993 Energy response of astronomical CCD x-ray detectors *SPIE* **1736** 138–48